Facile Synthesis of Gold Trisoctahedral Nanocrystals with Controllable Sizes and Dihedral Angles

Journal:	*Nanoscale*
Manuscript ID	NR-ART-04-2018-002949.R1
Article Type:	Paper
Date Submitted by the Author:	15-May-2018
Complete List of Authors:	Xia, Younan; Georgia Institute of Technology, The Wallace H. Coulter Department of Biomedical Engineering Huo, Da; Georgia Institute of Technology, Ding, Hong-ming; Soochow University, Zhou, Shan; School of Chemistry and Biochemistry, Georgia Institute of Technology, School of Chemistry & Biochemistry Li, Jun; Brookhaven National Laboratory Tao, Jing; Brookhaven National Laboratory, Center for Functional Nanomaterials Ma, Yu-qiang; Nanjing University, Department of Physics

SCHOLARONE™
Manuscripts

Facile Synthesis of Gold Trisoctahedral Nanocrystals with Controllable Sizes and Dihedral Angles

Da Huo,‡[a] Hongming Ding,‡[b] Shan Zhou,[c] Jun Li,[d] Jing Tao,[d] Yuqiang Ma,[*b] and Younan Xia[*a,c]

[a] *The Wallace H. Coulter Department of Biomedical Engineering, Georgia Institute of Technology and Emory University, Atlanta, Georgia 30332, USA*
E-mail: younan.xia@bme.gatech.edu

[b] *Center for Soft Condensed Matter Physics and Interdisciplinary Research, Soochow University, Suzhou, Jiangsu 215006, P. R. China*
E-mail: myqiang@nju.edu.cn

[c] *School of Chemistry and Biochemistry, Georgia Institute of Technology, Atlanta, Georgia 30332, USA*

[d] *Condensed Matter Physics and Materials Science Department, Brookhaven National Laboratory, Upton, New York 11973, USA*

‡ Author of equal contribution.

Abstract

Shape-controlled synthesis of Au nanocrystals is of paramount importance to their applications in plasmonics, catalysis, and nanomedicine. While the synthesis of Au nanocrystals enclosed by low-index facets has been greatly advanced over the past two decades, only limited progress has been made for their high-index counterparts. Here we report a robust route to the facile synthesis of Au trisoctahedral nanocrystals enclosed by high-index facets. Unlike the previously reported methods, our synthesis was conducted at room temperature, together with the introduction a new Au(III) precursor that was much harder to reduce than $AuCl_4^-$. In the setting of seed-mediated growth, the trisoctahedral nanocrystals could be readily prepared with sizes controllable from 20–80 nm and dihedral angles tunable in the range of 120–180 degrees. We further used computational modeling to demonstrate that the surface-functionalized Au trisoctahedral nanocrystal could outperform its spherical counterpart in terms of endocytic efficacy under identical conditions.

Introduction

Gold (Au) nanocrystals have been extensively explored for plasmonics, surface-enhanced Raman scattering (SERS),[1] biomedicine,[2] and photocatalysis[3] owing to their unique optical properties known as localized surface plasmon resonance (LSPR).[4] Considerable efforts have been directed to the synthesis of Au nanocrystals with controlled shapes or facets as these parameters have strong correlations with their optical and catalytic properties.[5] For instance, rod-shaped Au nanocrystals with aspect ratios (defined as the ratio of length to diameter) greater than two can feature strong LSPR in the spectral region from near-infrared to infrared (>650 nm) and thus shown great promise as a contrast agent and/or photothermal agent for biomedical applications.[6] On the other hand, Au nanocrystals with sharp tips, including nanostars[7] and nanoflowers[8] are favorable substrates for SERS because the local electromagnetic field around the tip can be several orders of magnitude greater than that on a flat surface.[1,9] In the case of heterogeneous catalysis, Au nanocrystals with high-index facets have been reported to show substantially enhanced catalytic and photocatalytic activities toward a variety of reactions.[10-12]

There is an extensive literature on the shape-controlled synthesis of Au nanocrystals enclosed by low-index facets such as {100}, {111}, and {110}, with notable examples including cubes, octahedrons, cuboctahedrons, and rhombic dodecahedrons.[13] When displaying a facet with at least one of the three Miller indices greater than one, the nanocrystals will be grouped into a different category known as high-index structures.[14] These nanocrystals possess abundant inadequately coordinated atoms at steps, edges, and kinks that often lead to enhancement in catalytic activity with respect to low-index facets. Though intriguing to catalytic application, the formation of high-index nanocrystals is not thermodynamically favored. The atoms at high-index facets, especially the adatoms, are much more vulnerable to atom deposition and further growth during a synthesis, in an effort to minimize the total surface free energy. As such, it is more challenging to generate Au nanocrystals enclosed by high-index facets with respect to their low-index counterparts.

It was not until recently that the first success of high-index Au nanocrystals in an aqueous system was reported.[15] In this case, Au trisoctahedral nanocrystals were produced through the reduction of $HAuCl_4$ by ascorbic acid (AA) under the protection of hexadecyl-trimethylammonium chloride (CTAC) at room temperature. The as-obtained Au trisoctahedrons were relatively large in size (>150 nm) and the sizes were rather polydispersed because self-

nucleation continuously occurred during the synthesis. In another study, Au trisoctahedral nanocrystals were observed as an intermediate when Au spherical seeds were directed to grow into rhombic dodecahedrons.[16] Overall, it is still a challenging task to produce Au trisoctahedral nanocrystals as uniform samples, together with controllable dihedral angles and compact sizes below 50 nm.[17-19]

In this study, we demonstrated, for the first time, that Au trisoctahedral nanocrystals with controllable sizes and dihedral angles (see Scheme 1 for definitions) could be synthesized through seed-mediated growth. Specifically, the sizes of the resultant nanocrystals can be controlled in the range of 20–80 nm. By varying the reaction temperature, we further demonstrated that the dihedral angle of the trisoctahedral nanocrystals could be tuned in the range of 120–180 degrees. In a proof-of-concept study, we used computational modeling to further demonstrate that the trisoctahedral nanocrystal could outperform the spherical counterpart in terms of endocytic efficacy. Collectively, this study demonstrates the promise of Au trisoctahedral nanocrystals as a new platform material for poential biomedical and catalytic applications.

Experimental section

Chemicals and materials

Gold(III) chloride trihydrate (HAuCl$_4$·3H$_2$O, >99.9%), ascorbic acid (AA, >99.0%), sodium borohydride (NaBH$_4$, 98%), hexadecyl-trimethylammonium chloride (CTAC, >98.0%), hexadecyl-trimethylammonium bromide (CTAB, >99%), and ethylenediaminetetraacetic acid disodium salt dehydrate (EDTA-2Na, 98%) were all obtained from Sigma-Aldrich (St. Louis, MO). Deionized (DI) water with a resistivity of 18.2 MΩ·cm at room temperature, which was prepared using a Millipore ultrapure water system (Billerica, MA), was used in all the experiments.

Synthesis of Au trisoctahedrons

We first synthesized 10-nm Au spherical seeds using a previously reported protocol.[20] Briefly, Au clusters were prepared by mixing 0.6 mL of ice-cold aqueous NaBH$_4$ (10 mM) with 5 mL of aqueous HAuCl$_4$ (0.25 mM) and 5 mL of aqueous CTAB (100 mM). The mixture was left undisturbed at 37 °C for 3 h to get rid of the remaining NaBH$_4$. For the synthesis of 10-nm Au

spheres, 2 mL of aqueous $HAuCl_4$ (0.5 mM), 2 mL of aqueous CTAC (200 mM), and 1.5 mL of aqueous AA (100 mM) were mixed in a 20-mL glass vial, followed by the introduction of 100 μL of the as-obtained Au clusters. The synthesis was allowed to proceed at room temperature for 10 min. The product was collected by centrifugation (15,000 rpm), washed once with water, and re-dispersed in aqueous CTAC (10 mM) to a final Au concentration of 17.3 μg/mL.

The EDTA-chelated Au(III) precursor (denoted as Au-EDTA) was prepared *via* a chelation reaction between equal molar amounts of EDTA-2Na and $HAuCl_4$ (10 mM), and diluted to a final concentration of 0.5 mM in terms of Au(III) for further use. In a standard synthesis of Au trisoctahedrons with a dihedral angel of 142 ± 8°, 4 mL of aqueous CTAC (100 mM) and 3 mL of Au-EDTA (0.5 mM) was mixed in a 20-mL glass vial under vigorous shaking at room temperature. Afterwards, 260 μL of freshly prepared aqueous AA (100 mM) was added, followed by the introduction of 25 μL of the as-obtained suspension of 10-nm Au spheres. The reaction was allowed to proceed on orbital shaker (250 rpm) for 20 min at room temperature. The as-obtained Au trisoctahedrons were collected *via* centrifugation (9,000 rpm) and washed three times with DI water to remove excess CTAC. For Au trisoctahedrons featuring dihedral angels of 128 ± 8°, 167 ± 6°, and 176 ± 4°, they were synthesized using the standard protocol except that the reaction temperature was changed from room temperature (21 ^{o}C) to 4, 50, and 90 ^{o}C, respectively.

Simulation model and method

The dissipative particle dynamics (DPD) simulations were applied to investigate the engulfment process of poly(ethylene glycol)-functionalized Au nanocrystals by plasma membranes. DPD is a coarse-grained simulation technique with hydrodynamic interaction.[21] The dynamics of the elementary units, which are the so-called DPD beads, is governed by Newton's equation of motion. Typically, there are three types of pairwise forces acting on bead i by bead j in the DPD: the conservative force, dissipative force, and random force. The conservative force $\boldsymbol{F}_{ij}^C = a_{ij}(1 - r_{ij})/r_c \cdot \boldsymbol{e}_{ij}$ is used to model the repulsive interaction between beads i and j, where $r_{ij} = |\boldsymbol{r}_{ij}|$ is the distance between the beads, $\boldsymbol{e}_{ij} = \boldsymbol{r}_{ij}/r_{ij}$ is the unit vector, r_c is the cutoff radius of the force, and a_{ij} represents the maximum repulsion interaction between beads i and j. For any two beads of the same type, we take the repulsive parameter $a_{ij} = 25k_BT/r_c$, and for any two beads of

different types, the interaction parameter a_{ij} can be calculated based on the Flory-Huggins interaction parameter χ_{ij}: $a_{ij} = a_{ii} + 3.497\chi_{ij}$, where χ_{ij} is determined by the solubility parameter difference between the beads. Besides, if the beads do not represent any specific type, a_{ij} is set to $25k_BT/r_c$ when the two beads are both hydrophilic or both hydrophobic; a_{ij} is set to $100k_BT/r_c$ when one is hydrophilic and the other is hydrophobic.[22] The detailed interaction parameters were shown below in Table 1. The dissipative force and random force serve as thermostat. In the present work, the long-ranged coulomb force was also included to take into account the electrostatic interactions between charged beads. Since the soft potential in the DPD allows for the overlap between DPD beads, this can lead to the formation of artificial ion pairs and cause divergence to the electrostatic potential when charged DPD beads are involved. To avoid this problem, we adopted a method from a previous report[23] by spreading out the charges using the distribution: $\rho_e(r) = \frac{3}{\pi r_e^3}(1 - \frac{r}{r_e})$ with $r < r_e$, where r_e is the electrostatic smearing radius and it is typically set as $1.6r_c$.

Table 1. Interaction parameters of bead-bead pairs a_{ij}. The G, P, S, L, H, T, W represent the Au nanocrystal bead, PEG bead, sulfur bead, ligand bead, lipid head bead, lipid tail bead, and water bead, respectively.

$a_{ij}(k_BT/r_c)$	G	P	S	L	H	T	W
G	25	100	5	100	100	25	100
P	100	25	25	25	26.3	100	26.3
S	5	25	25	25	26.3	100	26.3
L	100	25	25	25	26.3	100	26.3
H	100	26.3	26.3	26.3	25	100	25
T	25	100	100	100	100	25	100
W	100	26.3	26.3	26.3	25	100	25

Interaction of PEGylated nanoparticles with different cell membranes

The Au nanoparticle was fabricated by arranging DPD beads (G) on a face-centered cubic (*fcc*) lattice with a lattice constant of 0.33 nm into a desired geometric shape and volume, and all beads contained in

the nanoparticle moved as a rigid object. Specifically, here we considered a spherical nanocrystal and a trisoctahedral nanocrystal with a dihedral angle of $140°$. The PEG molecule was treated as a polymer with a number (N) of connective hydrophilic (P) beads in our simulations. To efficiently catch the major property of the PEG molecule, we adopted the coarse-grained model for PEG developed by Voth *et al.*,[24] *i.e.*, the neighboring beads on each PEG chain were connected by a harmonic bond $U_s = k_s(l - l_0)^2$, where $k_s = 3400 \ k_BT/nm^2$ is the spring constant and $l_0 = 0.34$ nm is the equilibrium bond length, indicating that the size of each PEG bead is about 0.34 nm. The angle potential formed by three adjacent beads is described by an angle potential $U_a = k_a(cos\theta - cos\theta_0)^2$, where $k_a = 17.1 \ k_BT$ is the angle potential constant, $\theta_0 = 130°$ is the equilibrium value of the angle. Besides, since there existed a lipid membrane in the present system, we chose a size of 10 nm for the nanocrystals. If we chose a size of 50 nm for the nanocrystals, the area of the membrane should be at least 20 times as large as the surface area of the nanocrystal (to avoid the finite size effect) and the size of the system box in X-Y dimension should be about 300 nm × 300 nm, which was far beyond our computing capability. For the same purpose, each PEG chain was set to compose of ten beads (N=10), and the last two beads (denoted as ligand beads, L) can interact with the receptors on the membrane *via* the soft Lennard-Jones (LJ) potential.

When modeling the cell membrane, we firstly used the charge-neutral lipid molecules that consisted of a head-group containing four connected hydrophilic beads (H) and two tails with three respective hydrophobic beads (T) to self-assemble into a lipid bilayer, where the first head bead carried a charge of +e, the second head bead carried a charge of -e, and the remaining two beads were kept neutral. The harmonic bond $U_s = k_s(l - l_0)^2$ ($k_s = 64k_BT/nm^2$, $l_0 = 0.5r_c$) between the neighboring beads was used to ensure the integrality of lipids. A weaker harmonic bond was inserted ($k_s = 10k_BT/nm^2$, $l_0 = 0.5r_c$) between the first hydrophobic beads on two tails of the lipid to keep the tails oriented along the same direction. We also used a three-body bond angle potential $U_a = k_a(1 - cos(\varphi - \varphi_0))$ ($k_a = 10k_BT$, $\varphi_0 = 180$) to depict the rigidity of lipid tails.[25] Besides, experimental results have shown that there are more anionic molecules (*e.g.*, phosphatidylserine and heparan sulfate proteoglycans) residing on the surface of cancer cells as compared to normal cells.[26] To mimic the negative charge property of cancer cells, here for the sake of simplicity, we set 10% of the lipid molecules as negatively charged ones in our simulations. And when modeling the negatively charged lipids, neutral hydrophilic bead was used to replace the first positively charged bead in the lipid molecule. Moreover, we also used a

simplified model (*i.e.*, the receptor-like lipid) to simulate the specific transmembrane protein, where the receptor-like lipid had the same conformation of lipid molecule, but its first two head beads were uncharged and can interact with the functional bead in PEG *via* soft LJ potentials. Since the receptors are usually over-expressed on the cancer cells while they are normally expressed on healthy cells, the percentage of the receptors in the cancer cell membrane and normal cell membrane was set as 50% and 10%, respectively.

In the simulations, the velocity-Verlet integration algorithm was used to update the coordination of each bead, where the integration time step Δt was 0.015τ. For the sake of simplicity, we chose the cutoff radius r_c, bead mass m, and energy k_BT as the simulation units. The size of initial simulation box was 80 nm × 80 nm × 40 nm with the number density of $\rho=3$. All simulations were performed in an NVT ensemble with temperature $k_BT = 1$, and the periodic boundary conditions were adopted in three directions. In order to keep the membrane surface under zero tension, we varied the box shape every 1000 time steps with the box volume fixed. The DPD units can be converted into SI units by mapping the membrane thickness and the lipid diffusion coefficient: $r_c= 1.0$ nm and $\tau = 2.4$ ns. All simulations in this section were carried out by using the modified soft package LAMMPS (1 Feb 2014).

Characterization

Transmission electron microscopy (TEM) images were taken on a JEOL-1400 microscope operated at 120 kV. High-resolution TEM images were captured on a JEOL-2100F microscope operated at 200 kV. The Au content in a sample was determined using an inductively-coupled plasma mass spectrometer (ICP-MS, NexION 300Q, PerkinElmer, Waltham, MA). All UV-vis spectra were recorded on a Cary 60 spectrometer (Agilent Technologies, Santa Clara, CA). The size and dihedral angle of the as-obtained nanocrystals were measured with Nanomeasure (version 1.2) and Digital Micrograph (Gatan), respectively, for nanocrystals projected along the <110> direction as shown in Scheme 1. The values from at least 80 such nanocrystals were averaged and presented as mean ± standard derivation.

Results and discussion
Seed-mediated synthesis of Au trisoctahedrons

As illustrated in Figure 1a, the Au trisoctahedral nanocrystals were synthesized in two steps. We first synthesized Au nanospheres (10 nm in diameter) *via* seed-mediated growth by following our previously reported protocol.[20] The Au nanospheres then served as seeds for another round of growth to generate trisoctahedral nanocrystals in the presence of AA and CTAC as the reductant and capping agent, respectively. Figure 1b shows TEM images of a typical sample of the Au trisoctahedrons prepared with a mean diameter of 45 nm and a dihedral angle of 142 ± 8° by following the standard protocol. We noticed that over 95% of the nanocrystals featured a concaved surface in six-fold symmetry, resembling the profile of a trisoctahedron projected along the <110> direction as illustrated in Figure 1a. The minor byproducts were mainly right bipyramids. As a major advantage over the protocols involving self-nucleation, seed-mediated growth concurrently minimizes the variations in size, shape, and morphology, contributing to the formation of uniform nanocrystals.

We further examined three of the particles (inset Figure 1b, labeled 1–3) in detail, and highlighted them in the right panels, together with corresponding atomic models projected along <111>, <110>, and <100> directions, respectively. The white dashed lines, representing the edges as illustrated in the atomic models, were shown to guide the eyes. We noticed that all these nanocrystals morphologically resemble the differently projected trisoctahedrons, except for the slight truncation observed at corners, an observation consistent with several previous reports.[15,16] Both surface diffusion of atoms and oxidative etching can contribute to the formation of truncated corners. Given that the synthesis was conducted at room temperature, we argued that surface diffusion should not play a major role. Therefore, we believed that the truncations at corners were likely caused by oxidative etching due to the presence of Cl^- and O_2 in the reaction solution. Compared to the atoms situated on a flat surface, those positioned at corners are less coordinated and thus more vulnerable to oxidative etching. This hypothesis is in agreement with our previous observation[27] in that Ag nanocubes with truncated corners tended to be formed in a reaction system containing both halide ions and O_2.

Next, we resolved the facet structures of an individual Au trisoctahedral nanocrystal using high-resolution TEM. Two adjacent facets in a valley, as highlighted in green and red colors in Figure 1c, were analyzed in detail. The boxed region was further magnified and shown in Figure 1d. The Miller indices of these two facets were calculated according to micro-facet notion theory.[28] Specifically, the corresponding facet highlighted in green color was comprised of a 7-

atom-wide (111) terrace and a 2-atom-wide (110) step, denoted by 7(111) × 2(110), collectively contributing to a high-index facet of {11 11 7}. Similarly, the one highlighted in red color, whose atomic arrangement could be interpreted as (111) × (110), was indexed as {331}. Furthermore, the Miller indices of another two facets enclosing the tip, highlighted by white dashed lines in Figure 1c, was resolved by measuring the curvature of the tip. Both facets could be indexed to be {221}. The two lattices with spacing of 2.37 and 1.49 Å, respectively, could be ascribed to {111} and {110} facets. Collectively, these findings demonstrate that the surface of a Au trisoctahedron is enclosed by a mix of different facets, with each one of them featuring a {*hhk*} (*h>k>0*)-analogous Miller index.

Tuning of the dihedral angle

One of the major differences that distinguishes our synthesis from the previous reports is the involvement of ethylenediaminetetraacetic acid (EDTA)-chelated Au^{3+} as the metal precursor.[29] This compound was initially introduced to slow down the rate of galvanic replacement between Au(III) metal precursor and Ag nanocubes in an effort to kinetically resolve the reaction using *in-situ* liquid cell TEM.[30] Here, we believed that the much greater constant of formation for the EDTA-Au^{3+} complex (K_f = 4.5 × 10^{34} M^{-1}) relative to that for the $AuCl_4^-$ complex (K_f = 2.0 × 10^{25} M^{-1}) would favor much slower reduction kinetics, contributing to the formation of kinetically controlled products. To test this hypothesis, we conducted experiments under identical conditions except for the type of Au(III) metal precursor. We analyzed the morphologies of nanocrystals synthesized in the presence of seeds differing in amount as shown in Figure 2. For seed-mediated growth, the size of the resultant nanocrystals is largely determined by the average number of atoms available for deposition onto an individual seed. As a result, the greater number of seeds involved should lead to the formation of products smaller in size. Although previous effort has been directed to the synthesis of Au trisoctahedral nanocrystals in the setting of seed-mediated growth,[16] that work only demonstrated the capability to control the size of octahedral products, not trisoctahedral intermediate. The lack of size-control, especially over the range below 50 nm, greatly impedes the application of Au trisoctahedral nanocrystals in both medicine and catalysis. As illustrated in Figure 2a-d, the size of the as-obtained Au trisoctahedrons could be reduced by increasing the amount of seeds while retaining the trisoctahedral morphology. Specifically, when 25 μL of seeds was used, we

obtained uniform Au trisoctahedral nanocrystals with a mean size of 78 ± 6 nm (Figure 2a). When we increased amount of the seeds to 100 μL (Figure 2b) and 300 μL (Figure 2c), the sizes decreased to 62 ± 7 nm and 28 ± 5 nm, respectively. In contrast, the use of an increased amount of seeds lead to the formation of a nearly spherical morphology when $HAuCl_4$ was used as the precursor (Figure 2e-h). Specifically, when the amount of seeds exceeded 200 μL, convex nanocrystals, instead of concaved ones, were obtained. We proposed that the slow reduction rate of EDTA-chelated Au^{3+},[30] assisted by the ability of CTA^+ to stabilize the high-index facets as reported in literature,[31] contributed to the preservation of trisoctahedral morphology during seeded growth.

The surface diffusion of the deposited atoms can also have a major impact on the evolution of shape or morphology during nanocrystal growth. The diffusion rate is mainly controlled by the reaction temperature,[32-34] with a lower temperature corresponding to a slower diffusion rate and thus the formation of a curved surface featuring a greater dihedral angle. To this end, we conducted the synthesis at different temperatures in the range of 0–90 °C. As shown in Figure 3, we were able to obtain a set of Au trisoctahedral nanocrystals featuring dihedral angles controlled at 128 ± 8° (4 °C), 142 ± 8° (21 °C, room temperature), 167 ± 6° (50 °C), and 176 ± 4° (90 °C), in good agreement with our expectation.[32-34] This result demonstrates the feasibility to control the dihedral angle by adjusting the reaction temperature. Specifically, for the nanocrystals featuring a dihedral angle of 128 ± 8° (Figure 3a), their structure is analogous to that of truncated octapods, which is rearely observed in a water-based synthesis. When the temperature was increased to 21 °C (Figure 3b) and 50 °C (Figure 3c), the concaveness of the as-obtained nanocrystals decreased accordingly. As reported in literature,[35] such a reduction could be attributed to the rearrangement of atoms on the corresponding facets, where the number of atoms on {110} facet at steps gradually surpassed that of atoms on {111} facet in terrace. This assumption was further validated by the morphology observed for nanocrystals obtained at 90 °C (Figure 3d). In this case, we obtained Au nanocrystals closely resembling rhombic dodecahedrons, a morphology enclosed exclusively by 12 {110} facets, showing the overwhelming presence of {110} facets.

We also analyzed the optical properties of the Au trisoctahedrons featuring different dihedral angles. As shown in Figure 4, all the trisoctahedral Au nanocrystal shown in Figure 3 feature LSPR peaks red-shifted relative to that of the spherical counterpart (534 nm). Specifically,

when the dihedral angle was increased, the resonance peak position was red-shifted from 540 nm (for 128 ± 8°) to 558 nm (for 176 ± 4°). Likely, it is the increasing dihedral angle that makes the nanocrystal more anisotropic in morphology, thus favoring a red shift for the surface plasmon resonance peak, a phenomenon well-established for explaining the correlation between the resonance peak position of Au nanorods and their aspect ratio.[6]

Investigation of nanocrystal-cell interaction

Gold nanocrystals have been extensively exploited as nanoscale carriers for a set of therapeutics, including small molecule drugs, proteins, and DNA or RNA.[2] Standing as the first hurdle faced by the nanocrystals is the impermeable plasma membranes associated with the cells. The cells have to uptake most the nanocrystals in an energy-dependent fashion owing to the lack of potential channels that allow for the passive diffusion of the nanocrystals. Nanocrystals with different shapes or morphologies are, therefore, expected to differ in endocytic efficacy by virtue of the fact that there exists a strong correlation between the shape or morphology of nanocrystals and their manners of interaction with cell membrane.[36] For instance, when interacting with cell membrane, independent of the presence of targeting ligand, the energy penalty for the internalization of anisotropic nanocrystals such as Au nanorods is much greater than their isotropic counterparts such as Au nanospheres.[37] On this basis, it is not surprising to witness the dominance of nanoscale carriers adopting a spherical or quasi-spherical shape.

Though successful to a certain extent, there is now evidence suggesting that most efficient cell uptake is not necessarily restricted to nanoparticles with a spherical shape only.[38] Since trisoctahedral nanocrystals have a relatively isotropic shape resembling that of nanospheres, we are interested in knowing if they could serve as an alternative to Au nanosphere in nanomedicine. As such, we investigated the interaction between Au nanocrystals (trisoctahedral or spherical shape) and cell membrane using computational modeling. Specifically, the trisoctahedral Au nanocrystals featuring a dihedral angle of 142 ± 8° were chosen for the modeling study because they could be synthesized at room temperature. To mimic the nanoscale carriers being used *in vitro*, both the trisoctahedral and spherical nanocrystals were functionalized with poly(ethylene glycol) (PEG) (see experimental section for the details of modeling),[39] as shown in Figure 5a and b, respectively. In an effort to provoke an active ligand-receptor-mediated endocytosis, the

anchored PEG chains was terminated by folic acid, whose receptor was expressed on several types of cancer cells at abnormally high level.[40]

As illustrated in Figure 5c, both the PEGylated trisoctahedral and spherical nanocrystals interact almost identically with plasma membrane expressing the folate receptor in terms of dynamics for endocytic vesicle formation. Upon the ligand-receptor recognition and subsequent binding, the membrane constantly bended inward, forming an unsealed vesicle encasing the nanocrystal. For simplicity, the uptake of an individual nanocrystal *via* endocytic vesicle was shown. In reality, multiple nanocrystals can be collectively imported through the same vesicle *in vitro*. As long as the energy released by nanocrystal-cell binding can sufficiently cover the expense of membrane bending, a transient internalization will proceed, and consequently end up with the total encasement of the engulfed-nanocrystal(s) with lipid vesicle. We noticed that both systems hold the promise for intracellular delivery. Besides, it could be observed that the two-way encasement from opposite directions was kind of advantageous for the formation of a vesicle containing a trisoctahedral nanocrystal (at 14.4 μs) with respect to the spherical counterpart (at 15.3 μs) at the late stage of engulfment. By contrast, for the cell membrane lacking folate receptor expression, we observed negligible endocytosis even over an extended period of time, regardless of the particle shape or morphology. This is of paramount significance for achieving selectivity toward specific cell line, in an effort to minimize the side-effect caused by off-target accumulation. Collectively, the simulation results clearly demonstrated that nanocrystals with a trisoctahedral shape could provoke endocytic response with an efficacy comparable to that of their spherical counterpart, if no better.

Conclusions

In summary, we have successfully synthesized Au trisoctahedral nanocrystals with sizes ranging from 20 to 80 nm by employing EDTA-chelated Au^{3+} as a new precursor. The dihedral angle of the as-obtained nanocrystals could also be manipulated in a controllable manner by changing the reaction temperature. In addition, we further demonstrated that the trisoctahedral nanocrystal with a dihedral angle of 142 ± 8° could undergo more rapid internalization by cells relative to its spherical counterpart. We believe this study would shed light on the significance of shape or morphology control in expanding and optimizing the applications of metal nanocrystal.

Conflicts of interest

The authors declare no competing financial interest.

Acknowledgements

References

(1)   S. Lal, N. K. Grady, J. Kundu, C. S. Levin, J. B. Lassiter, and N. J. Halas, *Chem. Soc. Rev.*, 2008, **37**, 898–911.

(2)   X. Yang, M. Yang, B. Pang, M. Vara, Y. Xia, *Chem. Rev.,* 2015, **115**, 10410−10488.

(3)   A. S. K, Hashmi and G. J. Hutchings, *Angew. Chem. Int. Ed.,* 2006, **45**, 7896–7936.

(4)   M. Hu, J. Chen, Z.-Y. Li, L. Au, G. V. Hartland, X. Li, M. Marquez, and Y. Xia, *Chem. Soc. Rev.*, 2006, **35**, 1084–1094.

(5)   K. L. Kelly, E. Coronado, L. L. Zhao, and G. C. Schatz, *J. Phys. Chem. B*, 2003, **107**, 668–677.

(6)   H. Chen, L. Shao, Q. Li, and J. Wang, *Chem. Soc. Rev.*, 2013, **42**, 2679–2724.

(7)   J. Chen, Z. Sheng, P. Li, M. Wu, N. Zhang, X.-F. Yu, Y. Wang, D. Hu, H. Zheng, and G. P. Wang, *Nanoscale*, 2017, **9**, 11888–11901.

(8)   V. M. Kariuki, J. C. Hoffmeier, I. Yazgan, and O. A. Sadik, *Nanoscale*, 2017, **9**, 8330–8340.

(9)   A. M. Jubb, Y. Jiao, G. Eres, S. T. Retterer, and B. Gu, *Nanoscale*, 2016, **8**, 5641–5648.

(10)   F.-S. Ke, B. Solomon, Y. Ding, G.-L. Xu, S.-G. Sun. Z. L. Wang, and X.-D. Zhou, *Nano Energy*, 2014, **7**, 179–188.

(11)   R. Rajendra, P. K. Gangadharan, S. Tripathi, S. Kurungot, and N. Ballav, *Nanoscale*, 2016, **8**, 19224–19228.

(12)   Z.-Y. Zhou, N. Tian, J.-T. Li, I. Broadwell, and S.-G. Sun, *Chem. Soc. Rev.*, 2011, **40**, 4167–4185.

(13)   H.-L. Wu, C.-H. Kuo, and M. H. Huang, *Langmuir*, 2010, **26**, 12307–12313.

(14)   Z. Quan, Y. Wang, and J. Fang, *Acc. Chem. Res.*, 2013, **46**, 191–202.

(15)   Y. Ma, Q. Kuang, Z. Jiang, Z. Xie, R. Huang, and L. Zheng, *Angew. Chem. Int. Ed.,* 2008,

47, 8901–8904

(16)   P.-J. Chung, L.-M. Lyu, and M. H. Huang, *Chem. - Eur. J.,* 2011, **17**, 9746–9752.

(17)   Y. Yu, Q. Zhang, X. Lu, and J. Y. Lee, *J. Phys. Chem. C* 2010, **114**, 11119–11126.

(18)   M. Eguchi, D. Mitsui, H.-L. Wu, R. Sato, and T. Teranishi, *Langmuir*, 2012, **28**, 9021–9026.

(19)   Y. Song, T. Miao, P. Zhang, C. Bi, H. Xia, D. Wang, and X. Tao, *Nanoscale*, 2015, **7**, 8405–8415.

(20)   Y. Zheng, X. Zhong, Z. Li, and Y. Xia., *Part. Part. Syst. Charact.,* 2014, **31**, 266–273.

(21)   R. D. Groot and P. B. Warren, *J. Chem. Phys.,* 1997, **107**, 4423–4435.

(22)   M. Dutt, O. Kuksenok, and A. C. Balazs, *Nanoscale,* 2013, **5**, 9773–9784.

(23)   R. D. Groot, *J. Chem. Phys.,* 2003, **118**, 11265–11277.

(24)   S. Izvekov and G. A. Voth, *J. Phys. Chem. B,* 2005, **109**, 2469–2473.

(25)   H. M. Ding, W. D. Tian, and Y. Q. Ma, *ACS Nano*, 2012, **6**, 1230–1238.

(26)   M. L. Jobin and I. D. Alves, *Biochimie*, 2014, **107**, 154–159.

(27)   S. Zhou, D. S. Mesina, M. A. Organt, T.-H. Yang, X. Yang, D. Huo, M. Zhao, and Y. Xia, *J. Mater. Chem. C*, 2018, **6**, 1384–1392.

(28)   M. A. Van Hove and G. A. Somorjai, *Sur. Sci.*, 1980, **92**, 489–518.

(29)   A. A. Cornejo, A. Castineiras, A. I. Yanovsky, and K. B. Nolan, *Inorg. Chim. Acta,* 2003, **349**, 91–96.

(30)   S. Tan, G. Lin, M. Bosman, U. Mirsaidov, and C. A. Nijhuis, *ACS Nano,* 2016, **10**, 7689–7695.

(31)   Y. W. Lee, M. Kim, S. W. Kang, and S. W. Han, *Angew. Chem. Int. Ed.,* 2011, **50**, 3466–3470

(32)   H. Zhang, M. Jin, and Y. Xia, *Angew. Chem. Int. Ed.,* 2012, **51**, 7656–7673.

(33)   Y. Xia, X. Xia, and H.-C. Peng, *J. Am. Chem. Soc.,* 2015, **137**, 7947–7966.

(34)   X. Xia, S. Xie, M. Liu, H.-C. Peng, N. Lu, J. M. Wang, J. Kim, and Y. Xia, *Proc. Natl. Acad. Sci. USA,* 2013, **110**, 6669–6673.

(35)   Z.-Y. Zhou, N. Tian, Z.-Z. Huang, D.-J. Chen, and S.-G. Sun, *Faraday Discuss.*, 2008, **140**, 81–92.

(36)   H. M. Ding and Y. Q. Ma, *Small*, 2015, **11**, 1055–1071.

(37)   Y. Li, M. Kröger, and W. K. Liu, *Nanoscale* 2015, **7**, 16631–16646.

(38)   K. Yang and Y.-Q. Ma, *Nat. Nanotech.*, 2010, **5**, 579–583.

(39)   A. L. Klibanov, K. Maruyama, V. P. Torchilin, and L. Huang, *FEBS Lett*. 1990, **268**, 235–237.

(40)   D. A. Silver, I. Pellicer, W. R. Fair, W. D. W. Heston, and C. Cordon-Cardo, *Clin Cancer Res.* 1997, **3**, 81–85.
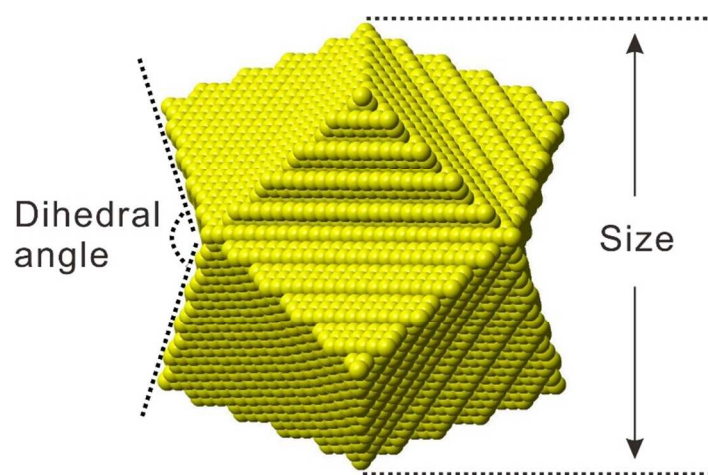
Scheme 1. A schematic illustration showing the definitions of size and dihedral angle for an individual Au trisoctahedron.
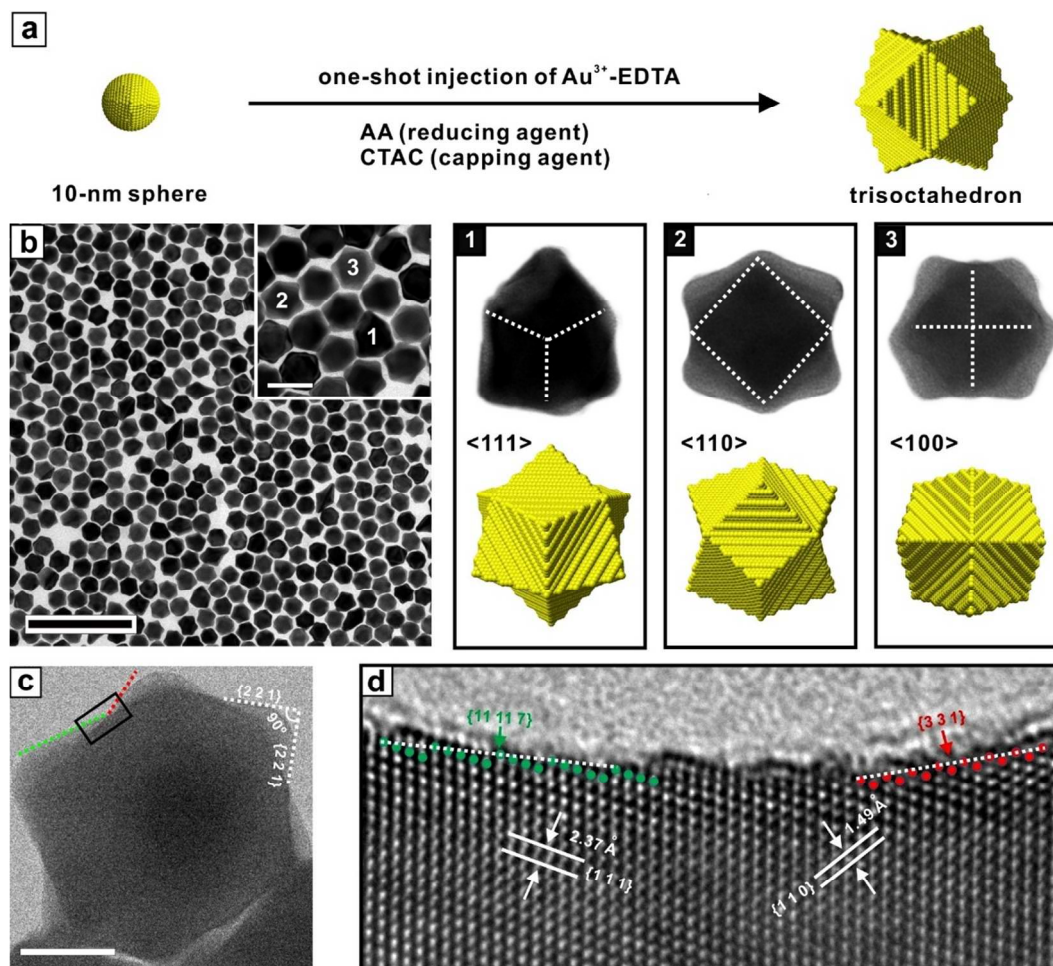
Figure 1. (a) Schematic illustration showing the growth of a Au trisoctahedron from a 10-nm Au spherical seed. (b) TEM images of the as-synthesized Au trisoctahedral nanocrystals at low and high (inset) magnifications. The right three panels show representative trisoctahedrons projected along <111>, <110>, and <100> directions, respectively, together with the corresponding atomic models. Scale bars: 200 nm and 50 nm (inset). (c) HRTEM image of an individual trisoctahedron oriented along <110> direction. Scale bar: 10 nm. (d) Atomic resolution TEM image taken from the region boxed in (c), showing the presence of {11 11 7} facet, denoted by 7(111) × 2(110), and {3 3 1} facet, denoted by (111) × (110). The atoms on {11 11 7} and {3 3 1} facets are marked in green and red colors, respectively.
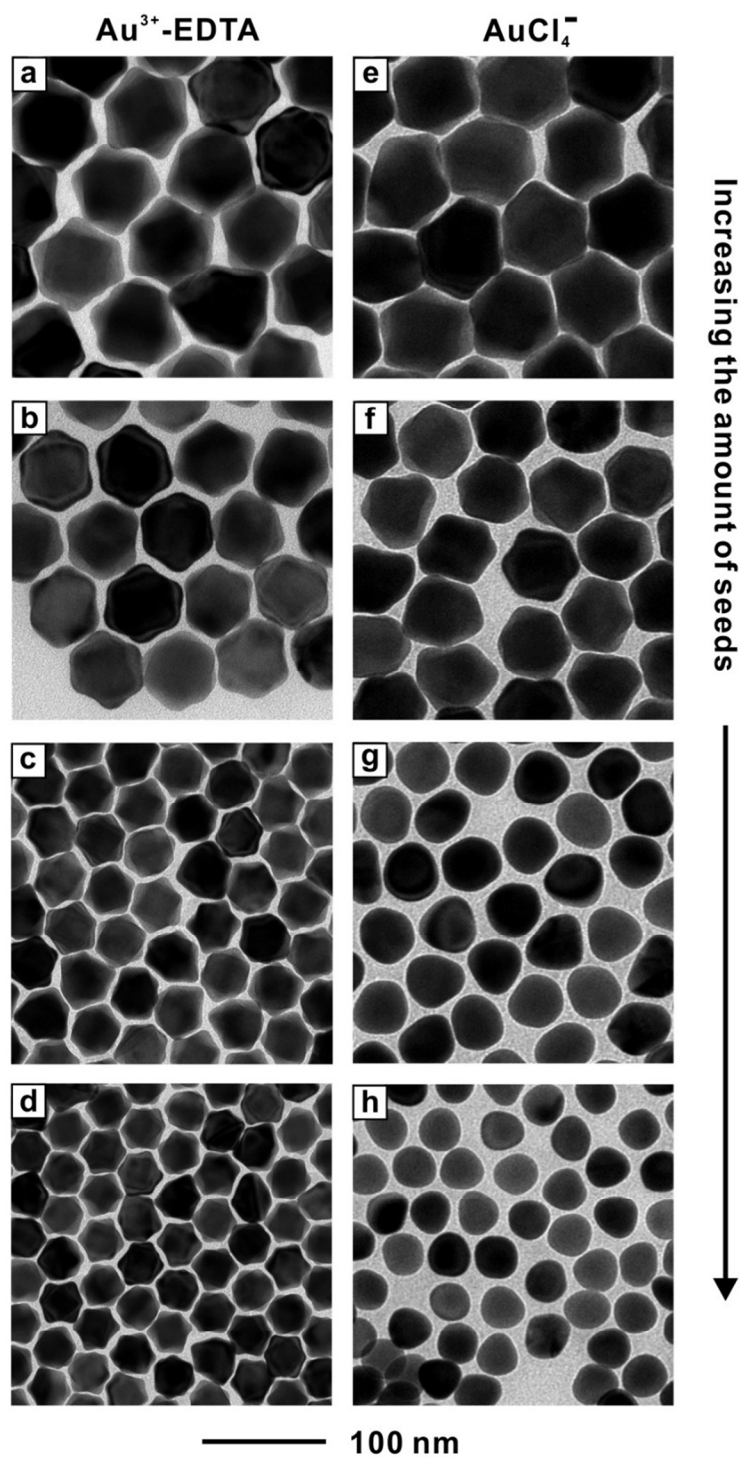
Figure 2. TEM micrographs of the as-obtained Au nanocrystals synthesized using (a-d) EDTA chelated-Au^{3+} or (e-h) $AuCl_4^-$ as a precursor under the standard conditions except for the amount of Au seeds: (a, e) 25, (b, f) 100, (c, g) 200, and (d, h) 300 μL. The scale bar applies to all images.
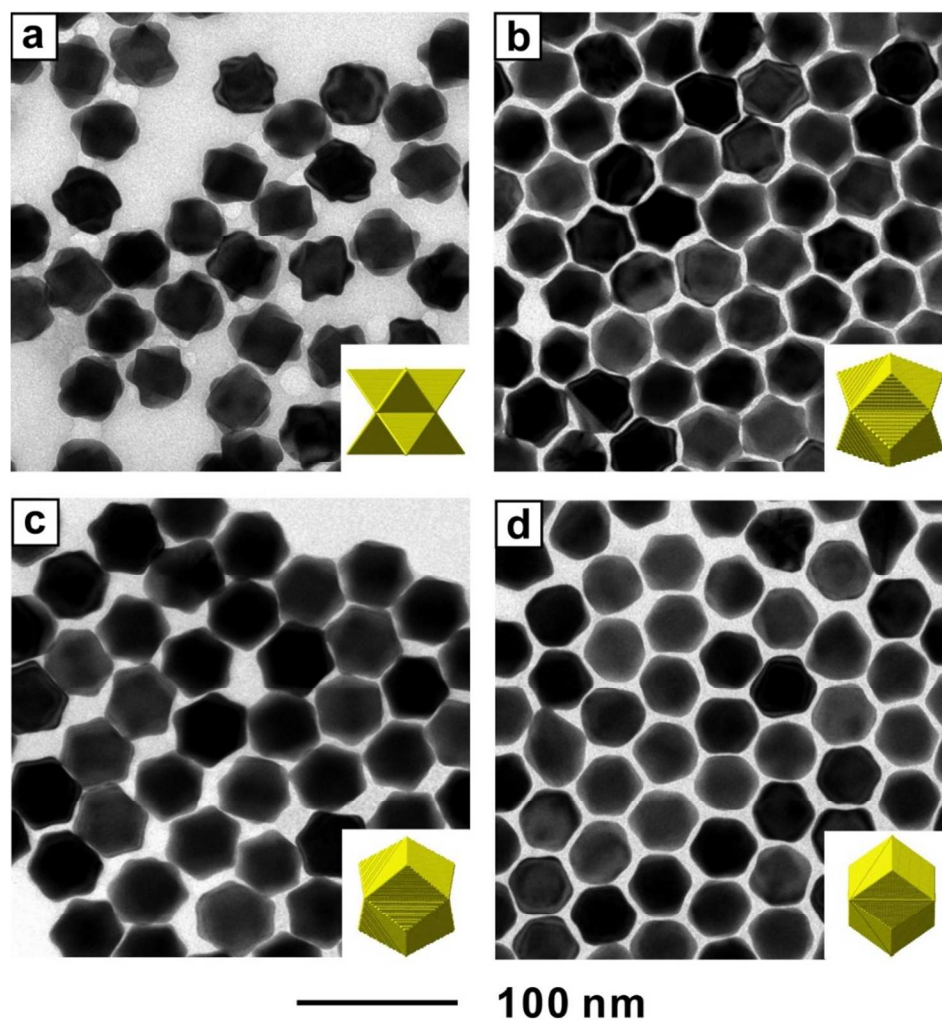
Figure 3. (a-d) TEM images of the as-obtained Au trisoctahedral nanocrystals featuring dihedral angels of (a) $128 \pm 8^{\circ}$, (b) $142 \pm 8^{\circ}$, (c) $167 \pm 6^{\circ}$, or (d) $178 \pm 4^{\circ}$. For the trisoctahedron featuring a dihedral angel close to 180°, the total number of facets is reduced from 24 to 12. The insets are atomic models showing the morphologies of trisoctahedrons featuring different dihedral angles. The scale bar applies to all images.
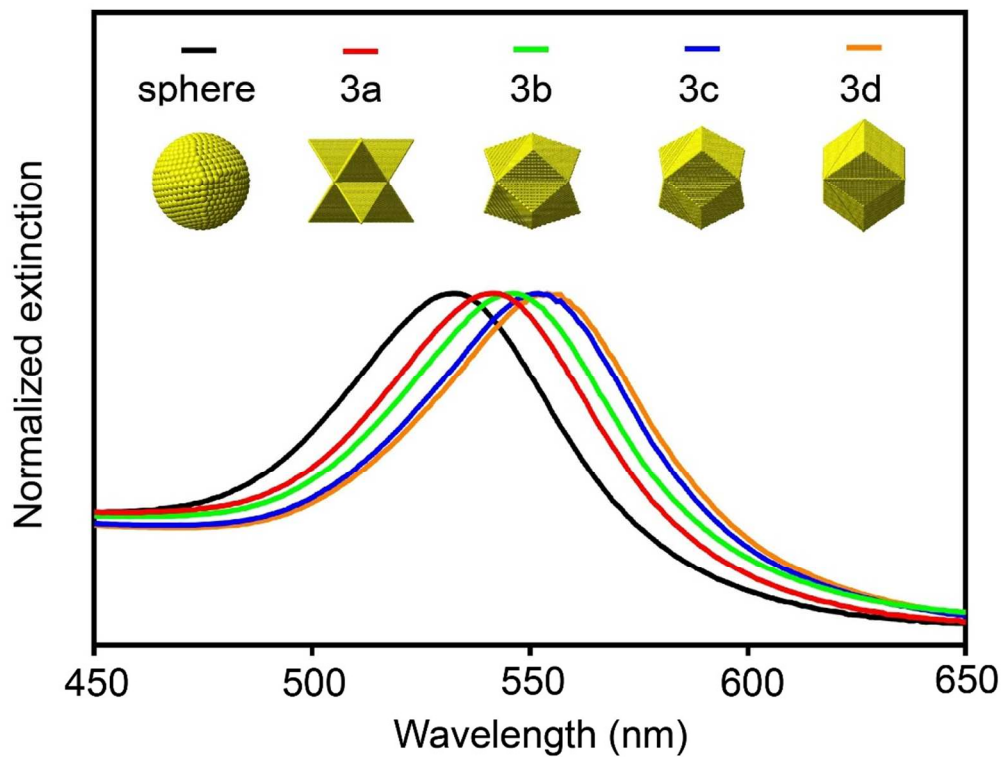
Figure 4. UV-vis spectra recorded from aqueous suspensions of the corresponding nanocrystals shown in Figure 3a-d, with 50-nm Au nanosphere serving as a reference. The extinction spectra are plotted by normalizing to the maximum extinction, and the atomic models are presented to help readers correlate the morphology with the corresponding extinction peak position.
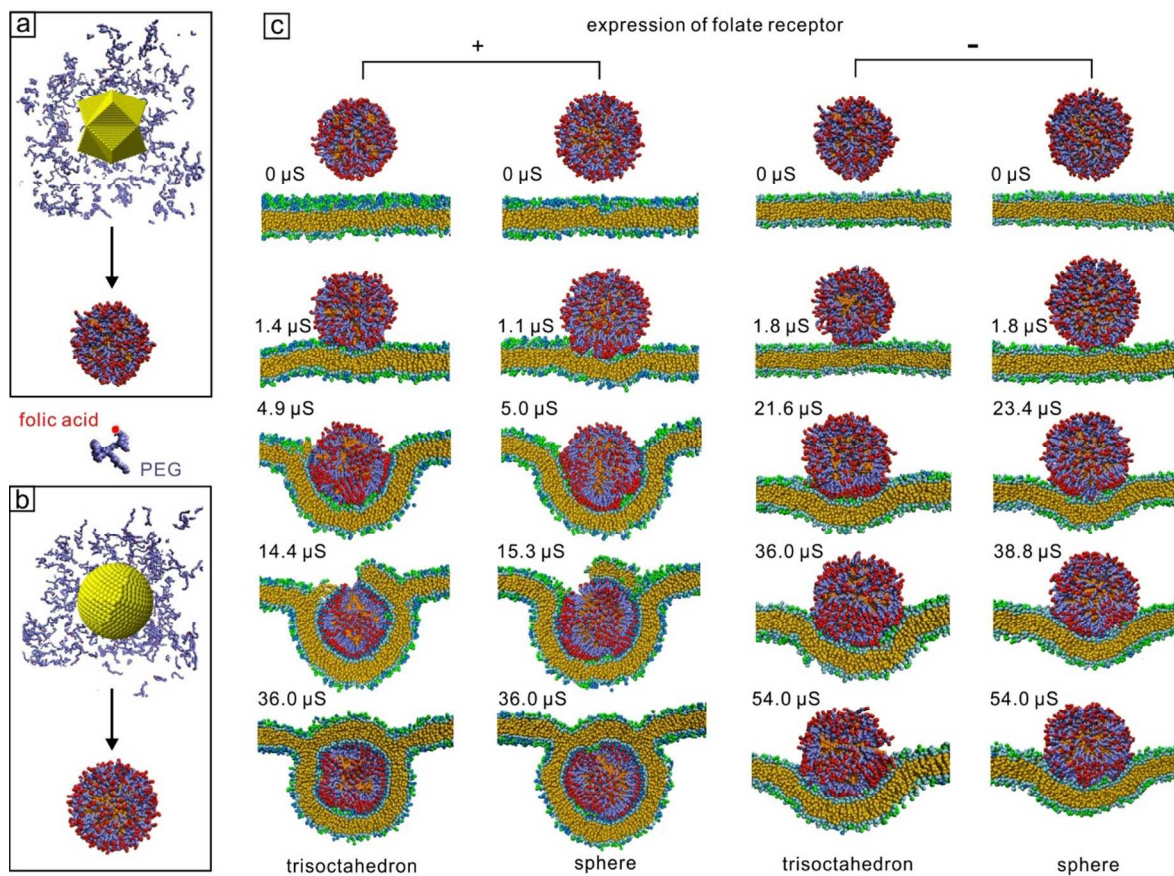
Figure 5. (a, b) Conjugation of folic acid-terminated PEG to the surface of 50-nm Au nanocrystals with (a) trisoctahedral (featuring a dihedral angle of $142 \pm 8°$) and (b) spherical shapes, respectively, as revealed by computational simulation. Representative model structure of folic acid-terminated PEG is shown in the middle, with red and violet beads stand for folic acid and the repeating unit of PEG, respectively. (c) Time-sequential snapshots showing the interactions between the PEGylated Au trisoctahedron (or sphere) and cell membranes positively (+) or negatively (-), respectively, expressing the folate receptor in a serum-free medium. The PEG chains were terminated in folic acid in all cases. To reduce the working load of simulation, the size of nanocrystals and length of ligand PEG were proportionally reduced.

Table of Contents
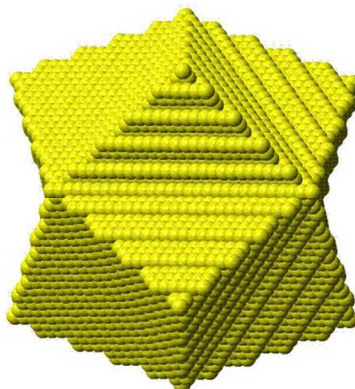
We demonstrate seed-mediated growth for the facile synthesis of Au trisoctahedral nanocrystals with tunable sizes and dihedral angles.